Globular cluster systems of relic galaxies

Karla A. Alamo-Martínez [1,2]★ Ana L. Chies-Santos [1] Michael A. Beasley [3]
Rodrigo Flores-Freitas [1] Cristina Furlanetto [4] Marina Trevisan,[1] Allan Schnorr-Müller [1]
Ryan Leaman [5] and Charles J. Bonatto [1]

[1]*Departamento de Astronomia, Instituto de Física, Universidade Federal do Rio Grande do Sul (UFRGS), Porto Alegre, R.S. 90040-060, Brazil*
[2]*Departamento de Astronomía, Universidad de Guanajuato, Apartado Postal 144, 36000 Guanajuato, Guanajuato, Mexico*
[3]*Instituto de Astrofísica de Canarias, Calle Vía Láctea, E-38205 La Laguna, Spain*
[4]*Departamento de Física, Instituto de Física, Universidade Federal do Rio Grande do Sul (UFRGS), Porto Alegre, R.S. 90040-060, Brazil*
[5]*Max-Planck Institut für Astronomie, Königstuhl 17, D-69117 Heidelberg, Germany*

ABSTRACT

We analyse the globular cluster (GC) systems of a sample of 15 massive, compact early-type galaxies (ETGs), 13 of which have already been identified as good relic galaxy candidates on the basis of their compact morphologies, old stellar populations and stellar kinematics. These relic galaxy candidates are likely the nearby counterparts of high-redshift *red nugget* galaxies. Using $F814W$ ($\approx I$) and $F160W$ ($\approx H$) data from the WFC3 camara onboard the *Hubble Space Telescope*, we determine the total number, luminosity function, specific frequency, colour, and spatial distribution of the GC systems (GCSs). We find lower specific frequencies ($S_N < 2.5$ with a median of $S_N = 1$) than ETGs of comparable mass. This is consistent with a scenario of rapid, early dissipative formation, with relatively low levels of accretion of low-mass, high-S_N satellites. The GC half-number radii are compact, but follow the relations found in normal ETGs. We identify an anticorrelation between the specific angular momentum (λ_R) of the host galaxy and the ($I - H$) colour distribution width of their GCSs. Assuming that λ_R provides a measure of the degree of dissipation in massive ETGs, we suggest that the ($I - H$) colour distribution width can be used as a proxy for the degree of complexity of the accretion histories in these systems.

Key words: galaxies: evolution – galaxies: formation – galaxies: star clusters: general.

1 INTRODUCTION

Massive early-type galaxies (ETGs) are host to some the most extreme formation events, and are the end products of complex processes such as gas accretion, *in situ* star formation, hierarchical merging, tidal interactions, and secular evolution (Trager et al. 2000; Thomas et al. 2005; La Barbera et al. 2013; Salvador-Rusiñol et al. 2020). ETGs experience dramatic size evolution over cosmic history (e.g. Trujillo et al. 2006; Buitrago et al. 2008; van Dokkum et al. 2010), have the most extreme initial mass functions (i.e. weighted to low-mass stars, van Dokkum & Conroy 2010; La Barbera et al. 2013), and host the most massive black holes in the Universe (Ferrarese & Merritt 2000; McConnell & Ma 2013). The rich variety of mechanisms that shape ETGs together with the fact that these galaxies contain ∼70 per cent of the total stellar budget in the local Universe (Fukugita, Hogan & Peebles 1998) turn these galaxies into attractive laboratories to test galaxy formation theories.

There is theoretical and observational evidence that massive ETGs ($M_* > 10^{11}$ M$_\odot$) in the local Universe have gone through two major formation phases (e.g. Hopkins et al. 2009; Oser et al. 2010; Hill et al. 2017). In the first phase, an *in situ* component is formed through dissipational processes, creating a massive and compact

central component. This first phase happens rapidly (< 1 Gyr) and early (at $z \gtrsim 2$) (Zolotov et al. 2015), and gives rise to a population of passively evolving objects seen at high redshift (Daddi et al. 2005; Schreiber et al. 2018; Valentino et al. 2020), sometimes termed 'red nuggets' (Damjanov et al. 2009). A second phase, dominated by minor mergers, then builds up predominantly the outer regions of ETGs (Naab, Johansson & Ostriker 2009; Johansson, Naab & Ostriker 2009). This process grows massive galaxies in size and mass, and presumably lowers their central densities (Hilz et al. 2012; Hilz, Naab & Ostriker 2013). Simulations suggest that the second phase may initially begin concurrently with the first, but continues to operate until the present day (e.g. Wellons et al. 2015; Furlong et al. 2017). For the purposes of this paper, we refer to an 'accretion event' as any merger that has occurred at $z < 2$.

A consequence of this formation pathway is that a small fraction of these red nuggets are expected to survive 'frozen' until the present-day Universe (Trujillo et al. 2009; Poggianti et al. 2013; Spiniello et al. 2020). These objects are thus considered relics of the first phase of ETG formation. In fact, such relic candidates have been reported to exist relatively nearby (Ferré-Mateu et al. 2017; Yıldırım et al. 2017; 2018). As relic galaxies, they are expected to have uniformly old stellar populations (>10 Gyr; Yıldırım et al. 2017), and be extremely compact, as is the case for the prototypical relic galaxy NGC 1277 (Trujillo et al. 2014) and also Mrk 1216 and PGC 032873 (Ferré-Mateu et al. 2017). In addition, stellar population studies indicate

★ E-mail: alrakomala@gmail.com

that relics such as NGC 1277 have extremely bottom-heavy stellar initial mass functions (IMFs) that do not vary with radius. This is consistent with the picture that this class of objects generally go on to form the central regions of massive ETGs (Martín-Navarro et al. 2015). Having accreted very few satelites, one might expect that relic galaxies would be found preferentially in relative isolation. However, a handful of relic candidates (Yıldırım et al. 2017) are found in the Perseus cluster. This result finds support in the work of Poggianti et al. (2013) and Peralta de Arriba et al. (2016), who find massive compact galaxies are preferentially found in central regions of the most dense environments. This may suggest that the conditions in early proto-clusters may have been especially favourable to preserve these systems. In the particular case of NGC 1277 in Perseus, it is possible that its proximity to NGC 1275 (Perseus A) has allowed NGC 1277 to evolve with little accretion. NGC 1275 may have acted (and continues to act) as a main attractor for any circumgalactic material.

Identification and characterization of relic galaxies is crucial to test the two-phase model, and offers the opportunity to study red nugget galaxies in the nearby Universe. In addition to the chemo-dynamical study of galaxy stellar populations, globular clusters (GCs) have proven to be uniquely powerful tools to trace the structure and history of galaxies (Brodie & Strader 2006; Pfeffer et al. 2018; Beasley 2020).

GC systems (GCSs) are generally thought to be old (most of them with ages >10 Gyr; Strader et al. 2005; Chies-Santos et al. 2011), and contain the imprints of the initial conditions of galaxy formation. GCSs of ETGs in the local Universe generally show complex colour distributions. Because GCs are generally old and co-eval, differences in colour are attributed to differences in metallicity, such that metal-poor GCs have 'blue' colours and metal-rich GCs are 'red'. This correspondence has been confirmed with spectroscopy (e.g. Beasley et al. 2008; Caldwell et al. 2011; Usher et al. 2012). Furthermore, the fraction of red GCs decreases as we move to lower galaxy luminosities, reaching the extreme faint of dwarfs that have predominantly blue GCs (e.g. Peng et al. 2006). This is explained by invoking the mass–metallicity relation where the metal-poor GCs are formed in low-mass galaxies, while the metal-rich GCs are formed in more massive proto-galaxies (Côté, Marzke & West 1998; Strader et al. 2005). In the two-phase galaxy formation context, the red metal-rich GCs are thought formed predominantly *in situ*, while an important fraction of blue, metal-poor GCs are accreted from dwarf galaxies.

Recently, Beasley et al. (2018) found that NGC 1277 contains almost exclusively red GCs suggesting that the galaxy has largely bypassed the second-phase of massive ETG formation, where ETG assembly should be dominated by minor merging events that would have brought in blue metal-poor GCs. The GC results for NGC 1277 suggest an accreted mass fraction of ∼12 per cent in this galaxy. In contrast, massive ETGs are generally estimated to have accreted somewhere between 50 and 90 per cent of their stars, with the rest comprising of an *in situ* component (Oser et al. 2010; Navarro-González et al. 2013).

Here, we present the first systematic study of GC populations in relic candidate galaxies. This paper is structured as follows. In Section 2, we introduce the data, photometric analysis, and GC candidates selection. In Section 3, we analyse the spatial distribution, luminosity function and total number of the GCSs. In Section 4, we look for correlations between the determined GCS properties and host galaxy properties from the literature, such as stellar mass, specific angular momentum, stellar velocity dispersion, and metallicity. In Section 5, we discuss and summarize the results.

2 DATA

In this work we analyse a sample of 15 massive, compact ETGs identified in the Hobby–Eberly telescope Massive Galaxy Survey (HetMGS; van den Bosch et al. 2015). Table 1 contains basic properties of our sample galaxies. These galaxies were initially selected in order to resolve their black hole 'sphere of influence', $r_i \equiv GM\sigma^{-2}$, where M is the black hole mass and σ is host galaxy velocity dispersion. Such a selection yields a strong bias in favour of massive, compact, and high-velocity-dispersion systems. Of the 15 HetMGS galaxies considered here, 13 have been identified as good relic galaxy candidates on the basis of their compact morphologies, old stellar populations, and stellar kinematics (Ferré-Mateu et al. 2017; Yıldırım et al. 2017). Their properties are very similar, though not as extreme, as the relic galaxy archetype NGC 1277 (Trujillo et al. 2014; Martín-Navarro et al. 2015; Beasley et al. 2018).

We use archival *Hubble Space Telescope* (*HST*) data from the programme GO: 13050 (PI: van den Bosch). The observations were taken with the WFC3 camera with the detectors UVIS (FOV 162 × 162 arcsec^2) and IR (FOV 123 × 136 arcsec^2) through filters *F814W* (≈*I*) and *F160W* (≈*H*), respectively. The data are homogeneous and all the targets have total integration time of 500 s for *I* and 1400 s for *H*. We downloaded the data from The Hubble Legacy Archive[1] that offers reduced data from *HST* following the standard procedure.

The FWHM for *I* and *H* are 0.1 and 0.22 arcsec, respectively. We use the AB photometric system, with zero-points in *I* and *H*, $zp_I = 25.12$ and $zp_H = 25.95$ mag, respectively. The Galactic extinction toward each galaxy in both bands are from Schlafly & Finkbeiner (2011). For consistency with Yıldırım et al. (2017), we adopt a cosmology with a Hubble constant of $H_0 = 70.5$ km s^{-1} Mpc^{-1}, a matter density of $\Omega_M = 0.27$, and dark energy density of $\Omega_\Lambda = 0.73$.

2.1 Photometry

In order to detect sources close to the centre of the galaxies, first we need to subtract the galaxy light. This is because the steepness of the galaxy luminosity is reflected as drastic changes in the background, hampering the detection of sources. To create the galaxy model, we use the tasks ELLIPSE and BMODEL from IRAF (Tody 1986) and fit elliptical isophotes to the surface brightness of the galaxies. For such procedure, we mask all the sources detected (except the galaxy to be fitted) using the SEGMENTATION MAP from a first SEXTRACTOR (Bertin & Arnouts 1996) run. We then create models for both *I* and *H* bands and subtract them from the original images.

When inspecting the subtracted images, we notice significant residuals in the central regions of most of the sample galaxies, which is mainly because of dust (disks or lanes) or complex structures like rings. Another manuscript is being drafted with an in-depth structural analysis of this sample of galaxies (Flores-Freitas, in preparation).

We perform source extraction on the galaxy subtracted image, by running SEXTRACTOR independently for each band with a set of parameters optimized for point source detection. We use a background grid size BACK_SIZE = 32 pixels and FILTERSIZE = 3 pixels, and an effective σ detection larger than 5 for both bands. Then, we apply a first cut to select objects with good quality in photometry by rejecting objects with saturated pixels, truncated by being close to the edges of the image, or, with magnitude error larger than 0.2 mag. Moreover, we estimate the concentration parameter

---

[1] https://hla.stsci.edu/

Table 1. Galaxy sample parameters.

Galaxy (1)	D (Mpc) (2)	ρ (#/Mpc^3) (3)	E (4)	$M_{V,\text{GAL}}$ (5)	A_V (6)	ap_c I (7)	ap_c H (8)
NGC 0384	59	0.08	Pair/group	−21.17	0.17	−0.18	−0.27
NGC 0472	74	3.17	–	−21.61	0.13	−0.15	−0.20
MRK 1216	94	0.11	–	−22.12	0.09	−0.18	−0.19
NGC 1270	69	7.76	Group/cluster Abell 426[a]	−21.85	0.45	−0.16	−0.19
NGC 1271	80	7.32	Group/cluster Abell 426	−22.04	0.45	−0.16	−0.18
NGC 1281	60	1.64	Group/cluster Abell 426	−21.26	0.46	−0.17	−0.17
NGC 1282	31	0.35	Group/cluster Abell 426	−20.32	0.46	−0.18	−0.20
UGC 2698	89	0.83	–	−22.36	0.40	−0.17	−0.18
NGC 2767	74	0.96	Group	−21.06	0.05	−0.20	−0.21
UGC 3816	51	0.27	Group	−21.66	0.17	−0.33	−0.24
NGC 3990	15	1.37	Pair/group	−18.95	0.05	−0.19	−0.25
PGC 11179	94	4.86	Group/cluster Abell 400	−21.70	0.51	−0.17	−0.24
PGC 12562	67	1.94	Group/cluster Abell 426	−20.95	0.46	−0.18	−0.30
PGC 32873	112	0.43	Pair	−22.12	0.04	−0.31	−0.23
PGC 70520	72	0.01	–	−21.75	0.26	−0.16	−0.19

Columns are as follows: (1) Galaxy name; (2) distance; (3) environment estimate – galaxy number density (ρ) within the volume containing the two closest neighbours; (4) environment according to NED; (5) integrated magnitude in the *V* band; (6) reddening; (7,8) aperture corrections in the *I* and *H* bands. [a] Perseus cluster.

C_{4-10}, which is the difference in magnitude within an aperture of 4 and 10 pixels in diameter, as it seems to be a better indicator of the luminosity profile for the faintest objects in comparison to the SEXTRACTOR CLASS_STAR parameter (Peng et al. 2011; Cho et al. 2016).

2.2 GC candidates selection

We use SEXTRACTOR output MAG_AUTO as the actual magnitude of the objects, but to estimate the colour we use aperture photometry within a radius of 4 pixels (0.16 arcsec) and apply the respective aperture correction. The aperture correction is estimated by constructing the curve of growth for multiple point sources, measuring the magnitude within different apertures (radius of 2, 4, 5, 8, 11, 14, 16 pixels) until it reaches a constant value, representing the total magnitude. Since our target galaxies are located at different distances, a fixed aperture corresponds to a different physical size at the source distance. In Table 1, we present the aperture corrections for each galaxy in the *I* and *H* bands. Finally, the sample of point sources that are taken as GC candidates are the ones detected independently in both bands (matching the coordinates within a radius <1 arcsec). Also, the GC candidates must have magnitudes according to the expected luminosity function of GCs (see Section 3.2 for more details), and colour $-0.5 < I - H < 1.5$, which is the expected colour for GCs (Cho et al. 2016).

In order to have an accurate estimation of the GC magnitude distribution and the total number of GCs for each galaxy, we need to determine the detection completeness curve as function of magnitude. To estimate the completeness curve, we construct the point spread function (PSF) using the TINY TIM [2] web interface. We add 20 000 artificial stars with a range in magnitude between 22 and 27 in both bands, and colour $I - H = 0$. We mimic the source detection as in the original images by applying the same source detection criteria in each band independently, and then select the ones that match in coordinates. We proceed by fitting a Pritchet function (Fleming et al. 1995) to the ratio of recovered to created artificial stars for the *I* band, as it is the band with reliable parameters

available for GC populations (Peng et al. 2011, Cho et al. 2016). As the observing strategy is the same for all the galaxies, the recovered parameters are similar but not exactly the same as the detection limit is affected by the brightness of the galaxy. The magnitude in the *I* band where 50 per cent of the artificial stars are recovered is in the range of 25.1 and 25.5, and with slopes in the range 3–5 for all the sample.

3 ANALYSIS

3.1 Spatial distribution of GC candidates

In order to estimate the amount of contaminants by Milky Way stars and background galaxies, and to quantify the spatial incompleteness, we parametrise the spatial distribution of the GC candidates by determining the surface number density of the GC candidates as function of radius. We measure the number of GC candidates inside circular concentric annuli with a constant width of 16 arcsec each, and normalise it by the effective area. We then fit a single Sérsic function (Sérsic 1968) including a background component:

$$\Sigma_{GC}(r) = \Sigma_0 \exp\left\{-b_n\left[\left(\frac{r}{R_{\text{e,GCS}}}\right)^{1/n_{\text{GCS}}} - 1\right]\right\} + BG_{\text{ps}}, \quad (1)$$

where $R_{\text{e,GCS}}$ is the radius that contains half of the GC population; Σ_0 is the surface number density at $R_{\text{e,GCS}}$; n_{GCS} is the Sérsic index; and BG_{ps} is the surface number density of background point sources. The fit is performed leaving all the parameters free but constraining n_{GCS} to be between 0.5 and 4, as are the expected values for disky and spheroidal galaxies (Kormendy et al. 2009), and $R_{\text{e,GCS}}$ to be larger than the effective radius of the galaxy ($R_{\text{e,GAL}}$) as the physical extension of the GCS is generally more extended than that of the starlight (Rhode et al. 2007; Kartha et al. 2014). The error bars are estimated assuming a poissonian error for the number of counts and weighted by the effective area. As an example, in Fig. 1, we show the GC surface number density for the galaxy NGC 1270, and its best Sérsic fit. For all the galaxies, we obtained $R_{\text{e,GCS}}$ between two and three times $R_{\text{e,GAL}}$, in agreement with the literature (Kartha et al. 2014; Forbes 2017; Hudson & Robison 2018). In Table 2, we present the measured $R_{\text{e,GCS}}$ values.
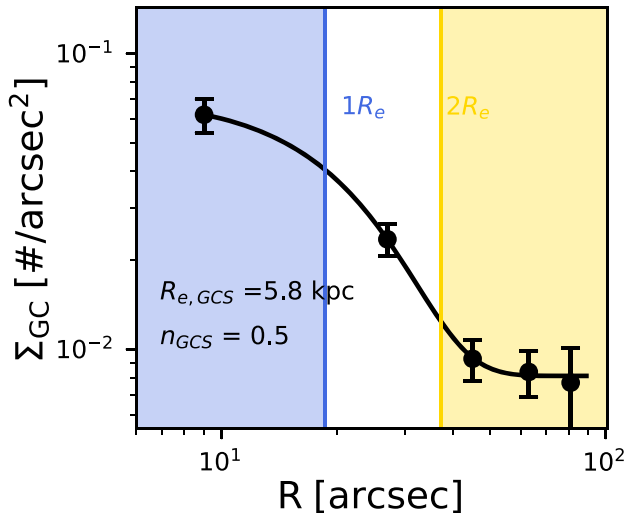
Figure 1. Surface number density of the GC candidates as function of radius for the galaxy NGC 1270. The error bars represent the Poissonian error for the number of counts and weighted by the effective area of each annulus. The solid line shows the best Sérsic fit. The blue shaded region shows the *inner* population that contains mostly GCs with high certainty, while the yellow shaded region shows the *outer* population that might be strongly affected by contaminants.

From inspection of the Sérsic fits, we define two subsamples: an *inner* population (sources within $1R_{e,GCS}$, blue shaded region in Fig. 1), whose sources with high certainty are dominated by GCs, and an *outer* population (sources out of $2R_{e,GCS}$, yellow shaded region in Fig. 1), which might be heavily contaminated by Milky Way stars and background galaxies. These subsamples are defined so that the inner subsample is well above the level of background contaminants.

3.2 Luminosity function and total GC number

The globular cluster luminosity function (GCLF) is a property that has been extensively studied among galaxies with different morphological type, mass and environment, being well described by a Gaussian (Harris 1991), albeit some departures form Gaussianity in the faint end (Jordán et al. 2007a), not relevant for this study. The peak or also called turnover (M^0) and width (σ^{GCLF}) of the GCLF are known to depend on the luminosity of the galaxy, where brighter turnover and broader distributions are observed in brighter galaxies (Kundu & Whitmore 2001; Jordán et al. 2006a). For ETGs, the values are $M_V^0 \approx -7.4$ and $M_I^0 \approx -8.5$ in the Johnson–Cousins photometric system. On the other hand, although σ^{GCLF} varies with the luminosity of the galaxy, it does not vary among bands (Kundu & Whitmore 2001), where, for the most massive galaxies, $\sigma_V^{GCLF} \approx 1.4$.

We adopt a GCLF turnover and width (AB system) dependent on the galaxy luminosity $M_{V,GAL}$ with the form:

$$M_I^0 = -7.4 + 0.04(M_{V,GAL} + 21.3) - 1.04 + 0.436, \quad (2)$$

$$\sigma_I^{GCLF} = 1.2 - 0.1(M_{V,GAL} + 21.3), \quad (3)$$

following (Jordán et al. 2006b; Villegas et al. 2010; Harris, Harris & Alessi 2013) on the dependence of M_V^0 as function of the galaxy luminosity, and assuming $M_V^0 - M_I^0 = 1.04$, which is a mean value measured for 28 ETGs according to Kundu & Whitmore (2001), and finally to convert from the Johnson–Cousins to AB photometric system, we add 0.436 (Sirianni et al. 2005).

Using this transformation, for a massive galaxy with $M_{V,GAL} \sim -24$ (as it is for M87) we recover $M_I^0 = -8.112$ in agreement with Jordán et al. (2007b). On the other hand, for dwarf galaxies with $M_{V,GAL} \sim -18$, we recover $M_I^0 = -7.872$ in agreement with Miller & Lotz (2007).

As mentioned in Section 2.2, we selected point sources fainter that $3\sigma_I^{GCLF}$ from M_I^0, together with a selection by colour $-0.5 < I - H < 1.5$ (Cho et al. 2016), in order to reduce the contamination by Milky Way stars and background galaxies.

To derive the GCLF of our studied galaxies, we estimate the luminosity function for the *inner* and *outer* subpopulations. This ultimately allows us to create an *inner* GCLF clean from contaminants. The luminosity function of the outer region (dominated by contaminants) is normalized to the area of the inner region, representing the luminosity function of contaminants. Then, our final GCLF for each galaxy is the luminosity function of the *inner* population minus the luminosity function of contaminants within $1R_{e,GCS}$, multiplied by 2, as within $1R_e$, we have half of the total population.

As the GCLF that we recover is the convolution of the intrinsic GCLF and the incompleteness Pritchet function (determined in Section 2.2), in order to obtain the total number of GCs, we estimate the area under the expected Gaussian GCLF by fitting the product of a Gaussian and the Pritchet function, with the expected σ_I^{GCLF} and M_I^0. In Fig. 2, we show the luminosity functions for the *inner* and *outer* subpopulations (top panel), as well as the GCLF (bottom panel) in the *I* band. We also show the best Gaussian∗Pritchet function (dotted curve), and the corresponding single Gaussian (solid curve) for the galaxy NGC 1270.

Although the data are relatively deep, it is not enough to sample the whole range of the GCLF, the faint limit we reach is about ~ 1 mag brighter than M_I^0 (depending on the distance to the galaxy). In Table 2, we show the total number of GCs corrected by incompleteness in area and photometry, and the corresponding error propagating the uncertainty in the fitted Gaussian amplitude.

4 RESULTS

In this section, we explore different correlations between the GCS and host galaxy parameters derived in this work and from the literature.

4.1 GC colour ($I - H$) correlations

The colours of the GC populations contain significant amounts of embedded information. They give us insights into ages and metallicities of the GCs (Brodie & Strader 2006), key parameters to infer the star formation history of the host galaxy. Spectroscopic analyses indicate that most GCs are old and co-eval (Cohen, Blakeslee & Côté 2003; Puzia et al. 2005; Beasley et al. 2008; Caldwell et al. 2011), implying that colour differences are mainly due to differences in metallicity. Unlike the relative homogeneity of the GCLF shape, the colour distribution of GCs shows more variety among different galaxies. In optical colours, more massive galaxies exhibit more complex GC colour distributions (dominated by bimodal distributions with different blue-to-red fractions; see Lee, Chung & Yoon 2019) and turn gradually unimodal with a blue dominant population as the mass of the galaxy decreases (Peng et al. 2006).

Even though the optical colors of GCSs have been extensively studied, their interpretation is still debated. Here, we do not attempt to study in detail the nature or the existence of bimodality of the near-IR colour distribution of GCs (for that, see Blakeslee et al. 2012; Chies-Santos et al. 2012; Cho et al. 2016) mainly because we are not

Table 2. GCS parameters.

Galaxy (1)	N_{GC} (2)	$R_{e,GCS}$(kpc) (3)	Σ_0 (4)	n_{mGCS} (5)	BG_{ps} (6)	S_N (7)	$\overline{I - H}$ [a] (8)	σ_{I-H} [a] (9)	Skewness[a,b] (10)	Detected/total (11)
NGC 0384	356 ± 47	6.04 ± 8.7	0.015	1.1	0.009	1.21	0.64	0.09	–	0.28
NGC 0472	328 ± 37	6.52 ± 0.8	0.021	0.5	0.003	0.74	0.59	0.11	–	0.23
MRK 1216	1013 ± 80	8.24 ± 0.7	0.034	0.5	0.003	1.43	0.59	0.10	−0.66	0.11
NGC 1270	485 ± 64	5.82 ± 0.8	0.032	0.5	0.008	0.88	0.78	0.13	−0.67	0.22
NGC 1271	180 ± 84	5.23 ± 1.1	0.018	0.7	0.003	0.27	0.69	0.09	–	0.22
NGC 1281	360 ± 30	4.5 ± 0.5	0.035	0.7	0.004	1.13	0.70	0.09	–	0.27
NGC 1282	184 ± 27	4.04 ± 1.5	0.017	0.6	0.005	1.37	0.58	0.11	–	0.82
UGC 2698	547 ± 100	8.57 ± 1.4	0.026	0.5	0.004	0.62	0.64	0.14	−0.59	0.18
NGC 2767	389 ± 49	7.96 ± 2.5	0.017	0.8	0.002	1.47	0.49	0.11	–	0.27
UGC 3816	253 ± 20	6.31 ± 2.5	0.017	0.8	0.004	0.55	0.51	0.09	0.47	0.49
NGC 3990	6 ± 2	1.6 ± 1.4	0.002	0.5	0.001	0.17	0.54	0.09	–	1.00
PGC 11179	200 ± 43	8.42 ± 3.0	0.005	0.5	0.003	0.42	0.65	0.10	−0.70	0.09
PGC 12562	31 ± 13	5.6 ± 8.8	0.004	0.5	0.007	0.13	0.84	0.21	–	0.44
PGC 32873	745 ± 238	18.4 ± 119.5	0.004	1.5	0.000	1.06	0.42	0.07	–	0.06
PGC 70520	183 ± 70	8.52 ± 2.4	0.007	0.5	0.003	0.36	0.51	0.08	–	0.26

Columns are as follows: (1) Galaxy name; (2) total number of GCs; (3) the radius that contains half of the GC population; (4) surface number density of GCs at $R_{e,GCS}$; (5) Sérsic index; (6) surface number density of background point sources; (7) specific frequency; (8) mean $I - H$; (9) standard deviation of $I - H$; (10) skewness of $I - H$; (11) fraction of detected to total GC number (after correction by incompleteness in area and photometry). [a] Measurements using all the GC candidate sources from 0 to $2R_{e,GCS}$, withouth background contamination subtraction.
[b] Values significantly different from zero at 95 per cent confidence level. Empty spaces are consistent with zero skew values.
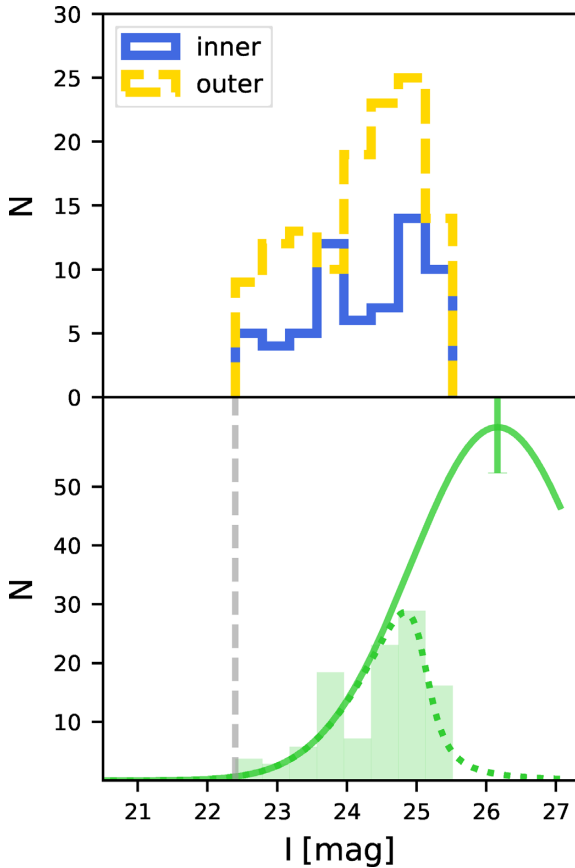
Figure 2. GC luminosity functions for galaxy NGC 1270. Top panel: luminosity function for the *inner* and *outer* subpopulations. Bottom panel: luminosity function of the *inner* population minus the luminosity function of contaminants within $1R_{e,GCS}$(corrected by area), multiplied by 2, as within $1R_e$, we have half of the total population. The dotted line shows the best Gaussian∗Pritchet function, the solid line is the corresponding single Gaussian, and the grey dashed vertical line indicates the bright cut for selected sources (M_I^0-$3\sigma_I^{GCLF}$).

sampling the entire population of GCs in any of the bands. Instead, we perform a rough characterization of the $I - H$ colour distribution of our sample by estimating the mean, the standard deviation, and the skewness of the GC candidates for each galaxy. The rationale here is that even such simple metrics can encode useful information about the GCSs and their host galaxies. In order to avoid outliers, we calculate the mean and standard deviation within interquartiles 1 and 3 for all the GC candidate sources (i.e. without background contamination subtraction), for the *inner* (within $1R_{e,GCS}$), *outer* outside $2R_{e,GCS}$, and from 0 to $2R_{e,GCS}$.

It is well known that the mean metallicity of a galaxy and its GCs increases for more massive galaxies (Kundu & Whitmore 2001; Usher et al. 2012 – and see the compilation in Beasley et al. 2019); together with the fact that the fraction of red GCs increases for brighter galaxies (Peng et al. 2006), we expect redder GCS colors for brighter galaxies. However, for a single galaxy, inner GCs have higher metallicities than the outer ones (Geisler, Lee & Kim 1996; Harris 2009); thus, in order to avoid a bias for selecting only the inner GCs, the GC colour of our sample is determined using the population from 0 to $2R_{e,GCS}$ where we have ∼90 per cent of the detected GC candidates. In Fig. 3, we show the colour $I - H$ distribution for galaxy NGC 1270, plotting the *inner*, *outer*, and from 0 to $2R_{e,GCS}$ subpopulations.

The skewness values reflect moderately skewed $I - H$ colour distributions for five galaxies, while for the rest of the sample galaxies, the colour distributions seem symmetrical (see Table 2). In Fig. 4, we plot the mean $I - H$ GCS colour versus galaxy metallicity and galaxy stellar mass ($\mathcal{M}_\star$) obtained from Yıldırım et al. (2017), where we can see a trend that more massive and metal-rich galaxies have GCs with on average redder mean $I - H$ colours, mimicking the effect of the GC peak metallicity, galaxy luminosity relation (see Brodie & Strader 2006). We also explore any dependence of the standard deviation of the $I - H$ GC colour with galaxy properties, identifying an interesting possible correlation when plotting it versus the stellar angular momentum, λ_R, from Yıldırım et al. (2017). We can see tantalizing evidence for an anti-correlation between λ_R and $I - H$ colour standard deviation. This trend may be explained in a
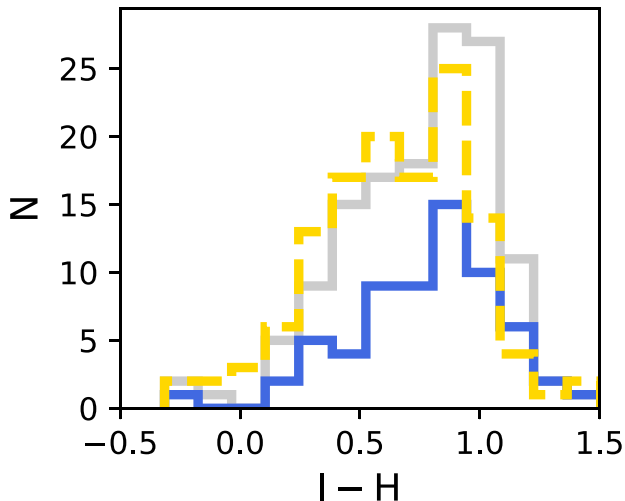
Figure 3. GC candidates colour $I - H$ distributions for the population within $1R_{e,GCS}$ (solid blue), outside $2R_{e,GCS}$ (dashed yellow), and from 0 to $2R_{e,GCS}$ (solid grey), for the galaxy NGC 1270.

hierarchical scenario where successive merging events decrease λ_R (Rodriguez-Gomez et al. 2017), while the final merged system, in turn, will tend to have a more complex, wider GC colour distribution. In this sense, the right-hand panel of Fig. 4 may show a progression of the 'degree of relicness' of a system, where the least evolved (most relic-like) systems will be located to the right-hand side of the plot with higher λ_R and a narrower colour width.

4.2 GC total number correlations

One of the first parameters defined to quantify the richness of a GC population is the called *specific frequency*, S_N (Harris & van den Bergh 1981), which is the number of GCs per unit galaxy luminosity, normalized to a galaxy with absolute V magnitude of -15:

$$S_N = 10^{0.4(M_{V,\text{GAL}}+15)}. \tag{4}$$

Harris & van den Bergh (1981) found values in the range $2 < S_N < 10$ for elliptical galaxies, noticing that the number of GCs do not scale with the luminosity of the galaxy. Since then, the S_N has been extensively studied among galaxies with different masses, morphological types, and environments (Harris & Harris 2001; Peng et al. 2008; Georgiev et al. 2010; Harris et al. 2013; Alamo-Martínez & Blakeslee 2017), where the behaviour of S_N as function of $M_{V,\text{GAL}}$ can be described by an U-shape, where S_N increases with luminosity on the bright side, and increases as the luminosity decreases on the faint side with a minimum of $S_N \sim 1$ for galaxies around $L_V^{\star}$, and large scatter on the edges.

The fact that the number of GCs seems to scale linearly with the halo mass of the host galaxy (Blakeslee 1999; Kravtsov & Gnedin 2005; Spitler & Forbes 2009; Hudson, Harris & Harris 2014; Boylan-Kolchin 2017; Harris, Blakeslee & Harris 2017; Choksi & Gnedin 2019; El-Badry et al. 2019) suggests that S_N scales inversely with the stellar-to-halo mass relation, or the total star formation efficiency, where high star formation efficiencies would imply low values of S_N. On the other hand, because S_N can be high in both giants and dwarf galaxies, but is uniformly low at the intermediate-mass regime, an explanation for the high S_N values in giant galaxies is that the large amounts of GCs are an accreted population that once belonged to dwarf galaxies. Recently, Beasley et al. (2018) reported that the GCS

of NGC 1277, in the Perseus cluster, is made up of almost exclusively red GCs, with only a small (<10 per cent) fraction of blue GCs by studying the optical colour $g - z$ with deep *HST* imaging. This finding supports the idea from other studies based on the age of its stellar population (Ferré-Mateu et al. 2018) and its IMF (Martín-Navarro et al. 2015) that this galaxy is a relic. Furthermore, the S_N of NGC 1277 is low (< 2), in accordance with a high star formation efficiency as would be for a rapidly early dissipative formation and a lack of a accretion of high-S_N, low-mass satellites.

In Fig. 5 (upper panel), we show S_N versus $M_{V,\text{GAL}}$ for our sample and the compilation of galaxies from Harris et al. (2013), which comprises a sample of 422 ETGs, S0s and late-type galaxies with $-24 < M_V < -14$. We find low values of S_N for our sample, < 2.5 with a median of 1. Assuming that the behaviour of the bright side of S_N versus $M_{V,\text{GAL}}$ plot is dominated by accretion, and that the faint side is consequence of dissipative processes, then relic galaxies would be the largest *seeds* formed by dissipative processes. A massive galaxy with low S_N could also be the consequence of a post-starburst due to a recent gas accretion with high luminosity dominated by young stellar population, as it seems to be the case for the second brightest galaxy in Fornax cluster (Liu et al. 2019).

A quantity harder to derive than S_N but with more physical meaning is the specific mass, S_M (Peng et al. 2008), which is the fraction of baryonic mass turned into GCs ($\mathcal{M}_{\text{GCS}}$):

$$S_M = 100 \frac{\mathcal{M}_{\text{GCS}}}{\mathcal{M}_{\text{baryonic}}}, \tag{5}$$

where for non-star-forming galaxies we can assume $\mathcal{M}_{\text{gas}} \sim 0$ and then $\mathcal{M}_{\text{baryonic}} \sim \mathcal{M}_{\star}$, valid for our sample of ETGs. As we know the total number of GCs, we just have to multiply by the mean GC mass, $\langle \mathcal{M}_{\text{GC}} \rangle$. As mentioned in Section 3.2, the mean and standard deviation of the GCLF depend on the luminosity of the galaxy, being brighter and broader as the galaxy luminosity increases. This is reflected in larger $\langle \mathcal{M}_{\text{GC}} \rangle$ for more luminous galaxies. By using the relation $M_V^0 = -7.4 + 0.04(M_{V,\text{GAL}} + 21.3)$ and $(M/L)_V = 2$ from Harris et al. (2013), we derive $\langle \mathcal{M}_{\text{GC}} \rangle$. To estimate the dynamical mass, we use

$$\mathcal{M}_{dyn} = \frac{4 R_{e,\text{GAL}} \sigma_e^2}{G}, \tag{6}$$

where $R_{e,\text{GAL}}$ is the effective radius of the galaxy, and σ_e is the stellar velocity dispersion within $R_{e,\text{GAL}}$, both obtained from Yıldırım et al. (2017). In Fig. 5 (bottom panel), we show S_M versus $\mathcal{M}_{dyn}$ for our sample and Harris et al. (2013) compilation.

Similar to the results for S_N, the relic galaxy sample lies below the relation for 'normal' mass-matched ETGs in the S_M–$\mathcal{M}_{dyn}$ plot. Again, this reinforces the notion that relic galaxies are maximally efficient in forming stars relative to GCs, and the process that might be responsible for lower this efficiency (i.e, satellite accretion) are less important in these galaxies.

By exploring the relation between N_{GC} and $\mathcal{M}_{dyn}$ for different morphological types, Harris et al. (2013) found that for ellipticals with $\mathcal{M} > 10^{10}$ M$_{\odot}$, the number of GCs increases almost in direct proportion to $\mathcal{M}_{dyn}$, while S0s and spirals show an offset of 0.2 and 0.3 dex, respectively, below the trend of ellipticals. They claim that for the same mass, the disky galaxies (higher angular momentum) have a lower fraction of GCs, or have higher fraction of field stars. Furthermore, Harris et al. (2013) found that $(R_{e,\text{GAL}}\sigma_e)^{1.3}$ is an accurate predictor of the total number of GCs over the entire mass range, from dwarfs to giants.

In Fig. 6, we show N_{GC} versus $\mathcal{M}_{dyn}$, $R_{e,\text{GAL}}$, σ_e, and $R_{e,\text{GAL}}\sigma_e$ for our sample and Harris et al. (2013) compilation without applying any
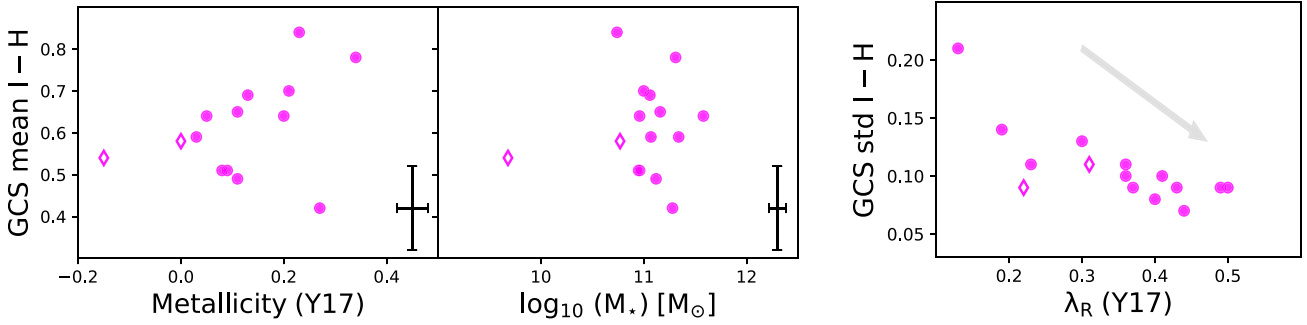
Figure 4. Mean and standard deviation of $I - H$ distributions within interquartiles 1 and 3 for all the GC candidate sources (i.e. without background contamination subtraction) within $2R_{e,GCS}$. Metallicity, $\mathcal{M}_\star$, and λ_R are from Yıldırım et al. (2017). The bottom right-hand panels shows the typical error bars. The dots are the galaxies classified as relics and the diamonds as non-relics by Yıldırım et al. (2017). The arrow indicates the direction at which the 'degree of relicness' of a given GCS increases (see the text for details).
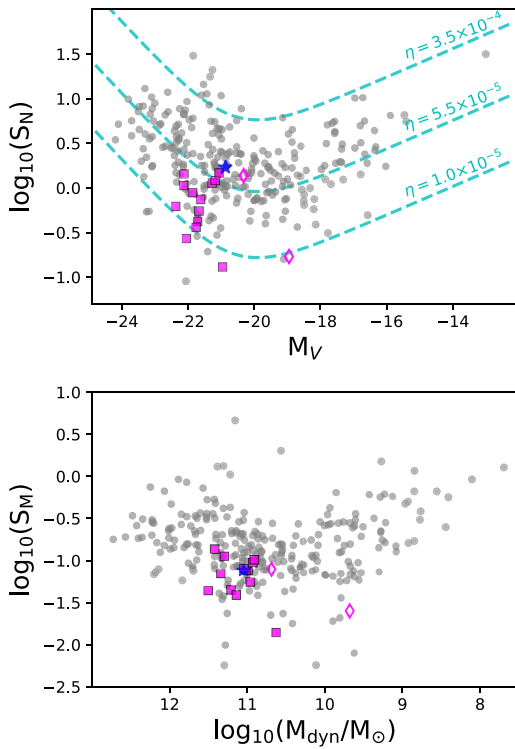
Figure 5. Upper panel: the specific frequency S_N as function of M_V with magenta squares representing our sample galaxies classified as relics and the diamonds as non-relics by Yıldırım et al. (2017), the grey dots are galaxies from literature (Harris et al. 2013), and the blue star is the galaxy NGC 1277 from Beasley et al. (2018). The dashed cyan lines represent predictions from Georgiev et al. (2010) assuming fixed GC formation efficiency η per total halo mass $\mathcal{M}_{Halo}$. Bottom panel: the specific mass S_M versus dynamical mass as derived from equation (6) (see the text).

offset according the morphological type as their Fig. 9. We can see that indeed, our sample, which is biased towards very high velocity dispersions, is dominated by low S_N values, which is a consequence of either a smaller fraction of GCs, or a higher fraction of field stars. Again, the minimal accretion of low-mass, high S_N satellites could result in this higher fraction of field stars. Nevertheless, it is worthwhile mentioning that the offset N_{GC} versus $\mathcal{M}_{dyn}$ for late-type galaxies versus ETGs could also be a direct result of using such a virial mass estimator. Late-type galaxies have far more of their orbital energy

tied up in rotationally supported orbits, so by using equation (6), we are likely to bias their dynamical mass estimates to the low side if we do not correct for this in a more detailed dynamical model.

4.3 GCS effective radius correlations

Numerical simulations predict that accreted stars are preferentially deposited at large galactocentric distances (Naab, Johansson & Ostriker 2009; Font et al. 2011; Navarro-González et al. 2013). This has been supported observationally from metallicity and age radial gradients (Pastorello et al. 2014; Greene et al. 2015), as well as kinematics and low-surface-brightness structures (e.g. Mackey et al. 2013). As the accreted galaxies not only contain stars but also GCs, the deposition of stars and GCs at large galactocentric distances causes increases in both $R_{e,GCS}$ and $R_{e,GAL}$.

Although $R_{e,GCS}$ is commonly measured to correct for spatial incompleteness, it is a GCS property little explored. Studies of the spatial extension of the GCS, measured as the radial distance at which the GC surface density reaches the background levels (Rhode et al. 2007; Rhode, Windschitl & Young 2010; Kartha et al. 2014) showed that the extension of the GCS is proportional to the host galaxy stellar mass and $R_{e,GAL}$ (but see also Saifollahi et al. 2020 for the case of ultradiffuse galaxies). However, as pointed out by Kartha et al. (2014), the extension of the GCS is strongly dependent on the quality of the data and the width of FOV, and claimed that the correlations should be considered more as a general trend than a quantitative relation. Similarly, studies of $R_{e,GCS}$ scaling relations (Forbes 2017; Hudson & Robison 2018) reported not unexpectedly correlations between $R_{e,GCS}$ and host galaxy properties. However, although the claim that $R_{e,GCS}$ scales with $R_{e,GAL}$ is inconsistent, the scaling factor is significantly different among authors.

In Fig. 7, we show $R_{e,GCS}$ as function of $R_{e,GAL}$ and stellar mass of the host galaxy for our sample and data from the literature. Our data follow the general trend where the spatial extension of the GCS is proportional to galaxy stellar mass and $R_{e,GAL}$ but with a closer distribution to ETGs in the Fornax galaxy cluster (Liu et al. 2019). We note that there is no evidence for stripping in these relic candidates, i.e. all of the correlations between the GC and system sizes reflect the co-evolution of both due to merging (or lack thereof) modulating the orbits/sizes of both the field stars and GCs.

5 CONCLUSIONS

In this study, we analyse the GCSs of a sample of 15 massive compact ETGs from which 13 are relic galaxy candidates
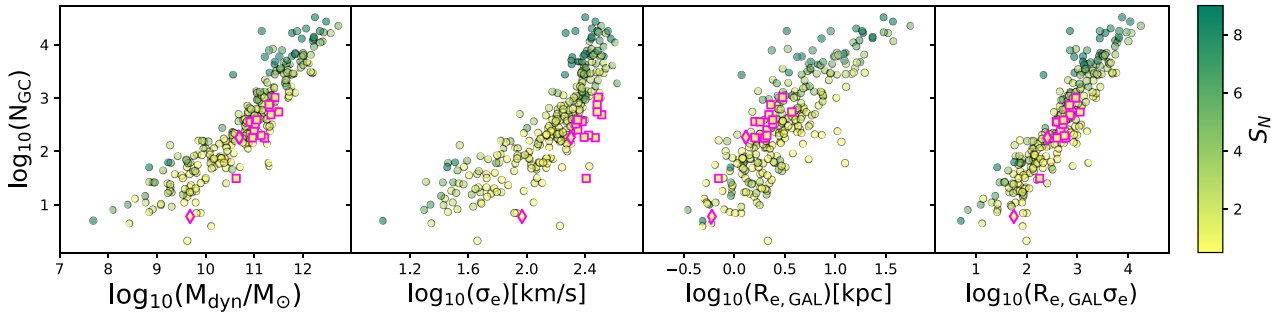
Figure 6. Number of GCs versus dynamical mass, velocity dispersion and effective radii of their host galaxies. Circles are from Harris et al. (2013), while the squares (relics) and diamonds (non-relics) are the galaxies studied in this work. The colour-code indicates the S_N.
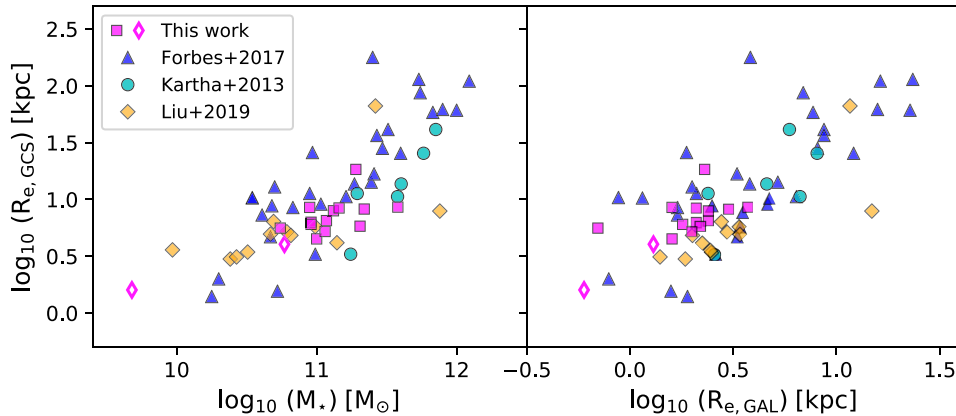

Figure 7. GCS effective radius, $R_{e,GCS}$, as function of stellar mass of the galaxy (left-hand panel) and $R_{e,GAL}$ (right-hand panel).

(Yıldırım et al. 2017). By using archival *HST* imaging in the *I* and *H* bands, we determine the GCLF, N_{GC}, colour, and spatial distribution of the GCS, S_N, S_M, and look for correlations with host galaxy properties from the literature, such as $\mathcal{M}_\star$, $\mathcal{M}_{dyn}$, λ_R, stellar velocity dispersion, and metallicity. Our main findings are as follows:

(i) The compact galaxy sample has low GC specific frequencies, $S_N < 2.5$ with a median of $S_N = 1$, whereas normal ETGs of the same mass typically have $2 < S_N < 10$. This is in agreement with the picture that the galaxies in our sample experienced high star formation efficiencies as would be the case for a rapid, early dissipative formation, together with relatively low levels of accretion of high-S_N, low-mass satellites.

(ii) The GCS spatial distributions are similar to those in normal ETGs in that they are more extended than the starlight, and $R_{e,GCS}$ correlates with the galaxy properties $R_{e,GAL}$, $\mathcal{M}_\star$, and $\mathcal{M}_{Halo}$.

(iii) Intriguingly, we find a mild, but significant anti-correlation between the standard deviation of the $I - H$ colour distribution and the galaxy specific angular momentum, λ_R. While the present data set is relatively small, if confirmed this result might be expected from hierarchical merging models whereby galaxies that have undergone less accretion/merging activity might be expected to preserve their initial λ_R and have less complex GCS colour distributions.

Future simulations can help constrain the diagnostic power of λ_R when allied to the width of the colour distributions of GCSs

for understanding of merger histories of galaxies. Moreover, quantification of the GC colour distributions of this sample with optical *HST* photometry would be extremely valuable to better constrain the accreted mass fractions in these systems.

Hubble Legacy Archive, which is a collaboration between the Space Telescope Science Institute (STScI/NASA), the Space Telescope European Coordinating Facility (ST-ECF/ESA) and the Canadian Astronomy Data Centre (CADC/NRC/CSA). We have made use of the NASA/IPAC Extragalactic Database, which is funded by the National Aeronautics and Space Administration and operated by the California Institute of Technology.

DATA AVAILABILITY

The data underlying this paper are available from the corresponding author, upon reasonable request.

REFERENCES

Alamo-Martínez K. A., Blakeslee J. P., 2017, ApJ, 849, 6
Beasley M. A., 2020, in Kabáth P., Jones D., Skarka M., eds, Reviews in Frontiers of Modern Astrophysics; From Space Debris to Cosmology, Springer International Publishing, Cham, p. 245
Beasley M. A., Bridges T., Peng E., Harris W. E., Harris G. L. H., Forbes D. A., Mackie G., 2008, MNRAS, 386, 1443
Beasley M. A., Trujillo I., Leaman R., Montes M., 2018, Nature, 555, 483
Beasley M. A., Leaman R., Gallart C., Larsen S. S., Battaglia G., Monelli M., Pedreros M. H., 2019, MNRAS, 487, 1986
Bertin E., Arnouts S., 1996, A&AS, 117, 393
Blakeslee J. P., 1999, AJ, 118, 1506
Blakeslee J. P., Cho H., Peng E. W., Ferrarese L., Jordán A., Martel A. R., 2012, ApJ, 746, 88
Boylan-Kolchin M., 2017, MNRAS, 472, 3120
Brodie J. P., Strader J., 2006, ARA&A, 44, 193
Buitrago F., Trujillo I., Conselice C. J., Bouwens R. J., Dickinson M., Yan H., 2008, ApJ, 687, L61
Caldwell N., Schiavon R., Morrison H., Rose J. A., Harding P., 2011, AJ, 141, 61
Chies-Santos A. L., Larsen S. S., Kuntschner H., Anders P., Wehner E. M., Strader J., Brodie J. P., Santos J. F. C., 2011, A&A, 525, A20
Chies-Santos A. L., Larsen S. S., Cantiello M., Strader J., Kuntschner H., Wehner E. M., Brodie J. P., 2012, A&A, 539, A54
Cho H., Blakeslee J. P., Chies-Santos A. L., Jee M. J., Jensen J. B., Peng E. W., Lee Y.-W., 2016, ApJ, 822, 95
Choksi N., Gnedin O. Y., 2019, MNRAS, 488, 5409
Cohen J. G., Blakeslee J. P., Côté P., 2003, ApJ, 592, 866
Côté P., Marzke R. O., West M. J., 1998, ApJ, 501, 554
Daddi E. et al., 2005, ApJ, 626, 680
Damjanov I. et al., 2009, ApJ, 695, 101
El-Badry K., Quataert E., Weisz D. R., Choksi N., Boylan-Kolchin M., 2019, MNRAS, 482, 4528
Ferrarese L., Merritt D., 2000, ApJ, 539, L9
Ferré-Mateu A., Trujillo I., Martín-Navarro I., Vazdekis A., Mezcua M., Balcells M., Domínguez L., 2017, MNRAS, 467, 1929
Ferré-Mateu A., Forbes D. A., Romanowsky A. J., Janz J., Dixon C., 2018, MNRAS, 473, 1819
Fleming D. E. B., Harris W. E., Pritchet C. J., Hanes D. A., 1995, AJ, 109, 1044
Font A. S., McCarthy I. G., Crain R. A., Theuns T., Schaye J., Wiersma R. P. C., Dalla Vecchia C., 2011, MNRAS, 416, 2802
Forbes D. A., 2017, MNRAS, 472, L104
Fukugita M., Hogan C. J., Peebles P. J. E., 1998, ApJ, 503, 518
Furlong M. et al., 2017, MNRAS, 465, 722
Geisler D., Lee M. G., Kim E., 1996, AJ, 111, 1529
Georgiev I. Y., Puzia T. H., Goudfrooij P., Hilker M., 2010, MNRAS, 406, 1967
Greene J. E., Janish R., Ma C.-P., McConnell N. J., Blakeslee J. P., Thomas J., Murphy J. D., 2015, ApJ, 807, 11
Harris W. E., 1991, ARA&A, 29, 543

Harris W. E., 2009, ApJ, 699, 254
Harris W. E., Harris G. L. H., 2001, AJ, 122, 3065
Harris W. E., van den Bergh S., 1981, AJ, 86, 1627
Harris W. E., Harris G. L. H., Alessi M., 2013, ApJ, 772, 82
Harris W. E., Blakeslee J. P., Harris G. L. H., 2017, ApJ, 836, 67
Hill A. R. et al., 2017, ApJ, 837, 147
Hilz M., Naab T., Ostriker J. P., Thomas J., Burkert A., Jesseit R., 2012, MNRAS, 425, 3119
Hilz M., Naab T., Ostriker J. P., 2013, MNRAS, 429, 2924
Hopkins P. F., Bundy K., Murray N., Quataert E., Lauer T. R., Ma C.-P., 2009, MNRAS, 398, 898
Hudson M. J., Robison B., 2018, MNRAS, 477, 3869
Hudson M. J., Harris G. L., Harris W. E., 2014, ApJ, 787, L5
Johansson P. H., Naab T., Ostriker J. P., 2009, ApJ, 697, L38
Jordán A. et al., 2006a, ApJ, 651, L25
Jordán A. et al., 2006b, ApJ, 651, L25
Jordán A. et al., 2007a, ApJS, 171, 101
Jordán A. et al., 2007b, ApJS, 171, 101
Kartha S. S., Forbes D. A., Spitler L. R., Romanowsky A. J., Arnold J. A., Brodie J. P., 2014, MNRAS, 437, 273
Kormendy J., Fisher D. B., Cornell M. E., Bender R., 2009, ApJS, 182, 216
Kravtsov A. V., Gnedin O. Y., 2005, ApJ, 623, 650
Kundu A., Whitmore B. C., 2001, AJ, 121, 2950
La Barbera F., Ferreras I., Vazdekis A., de la Rosa I. G., de Carvalho R. R., Trevisan M., Falcón-Barroso J., Ricciardelli E., 2013, MNRAS, 433, 3017
Lee S.-Y., Chung C., Yoon S.-J., 2019, ApJS, 240, 2
Liu Y., Peng E. W., Jordán A., Blakeslee J. P., Côté P., Ferrarese L., Puzia T. H., 2019, ApJ, 875, 156
Mackey A. D. et al., 2013, MNRAS, 429, 281
Martín-Navarro I., La Barbera F., Vazdekis A., Ferré-Mateu A., Trujillo I., Beasley M. A., 2015, MNRAS, 451, 1081
McConnell N. J., Ma C.-P., 2013, ApJ, 764, 184
Miller B. W., Lotz J. M., 2007, ApJ, 670, 1074
Naab T., Johansson P. H., Ostriker J. P., 2009, ApJ, 699, L178
Navarro-González J., Ricciardelli E., Quilis V., Vazdekis A., 2013, MNRAS, 436, 3507
Oser L., Ostriker J. P., Naab T., Johansson P. H., Burkert A., 2010, ApJ, 725, 2312
Pastorello N., Forbes D. A., Foster C., Brodie J. P., Usher C., Romanowsky A. J., Strader J., Arnold J. A., 2014, MNRAS, 442, 1003
Peng E. W. et al., 2006, ApJ, 639, 95
Peng E. W. et al., 2008, ApJ, 681, 197
Peng E. W. et al., 2011, ApJ, 730, 23
Peralta de Arriba L., Quilis V., Trujillo I., Cebrián M., Balcells M., 2016, MNRAS, 461, 156
Pfeffer J., Kruijssen J. M. D., Crain R. A., Bastian N., 2018, MNRAS, 475, 4309
Poggianti B. M., Moretti A., Calvi R., D'Onofrio M., Valentinuzzi T., Fritz J., Renzini A., 2013, ApJ, 777, 125
Puzia T. H., Kissler-Patig M., Thomas D., Maraston C., Saglia R. P., Bender R., Goudfrooij P., Hempel M., 2005, A&A, 439, 997
Rhode K. L., Zepf S. E., Kundu A., Larner A. N., 2007, AJ, 134, 1403
Rhode K. L., Windschitl J. L., Young M. D., 2010, AJ, 140, 430
Rodriguez-Gomez V. et al., 2017, MNRAS, 467, 3083
Saifollahi T., Trujillo I., Beasley M. A., Peletier R. F., Knapen J. H., 2020, MNRAS, preprint (arXiv:2006.14630)
Salvador-Rusiñol N., Vazdekis A., La Barbera F., Beasley M. A., Ferreras I., Negri A., Dalla Vecchia C., 2020, Nat. Astron., 4, 252
Schlafly E. F., Finkbeiner D. P., 2011, ApJ, 737, 103
Schreiber C. et al., 2018, A&A, 618, A85
Sersic J. L., 1968, Atlas de Galaxias Australes, Atlas de Galaxias Australes, Observatorio Astronómico de Cordoba, Argentina
Sirianni M. et al., 2005, PASP, 117, 1049
Spiniello C. et al., 2020, ApJ, 646, 19
Spitler L. R., Forbes D. A., 2009, MNRAS, 392, L1
Strader J., Brodie J. P., Cenarro A. J., Beasley M. A., Forbes D. A., 2005, AJ, 130, 1315

Thomas D., Maraston C., Bender R., Mendes de Oliveira C., 2005, ApJ, 621, 673

Tody D., 1986, in Crawford D. L., ed., Proc. SPIE Conf. Ser. Vol. 627, Instrumentation in Astronomy VI. SPIE, Bellingham, p. 733

Trager S. C., Faber S. M., Worthey G., González J. J., 2000, AJ, 119, 1645

Trujillo I. et al., 2006, ApJ, 650, 18

Trujillo I., Cenarro A. J., de Lorenzo-Cáceres A., Vazdekis A., de la Rosa I. G., Cava A., 2009, ApJ, 692, L118

Trujillo I., Ferré-Mateu A., Balcells M., Vazdekis A., Sánchez-Blázquez P., 2014, ApJ, 780, L20

Usher C. et al., 2012, MNRAS, 426, 1475

Valentino F. et al., 2020, ApJ, 889, 93

van den Bosch R. C. E., Gebhardt K., Gültekin K., Yıldırım A., Walsh J. L., 2015, ApJS, 218, 10

van Dokkum P. G. et al., 2010, ApJ, 709, 1018

van Dokkum P. G., Conroy C., 2010, Nature, 468, 940

Villegas D. et al., 2010, ApJ, 717, 603

Wellons S. et al., 2015, MNRAS, 449, 361

Yıldırım A., van den Bosch R. C. E., van de Ven G., Martín-Navarro I., Walsh J. L., Husemann B., Gültekin K., Gebhardt K., 2017, MNRAS, 468, 4216

Zolotov A. et al., 2015, MNRAS, 450, 2327

APPENDIX A: INDIVIDUAL GC SYSTEMS (GCS)

In Figs A1–A15, we show for each individual GCS several derived properties: the spatial distribution of the GC candidates, the surface number density of the GC candidates as function of radius with the best Sérsic fit, the $I - H$ colour distributions for the population at different galactocentric radii, the I-band luminosity function, the H-band luminosity function of the GC candidates within $2R_e$ and the $I - H$ colour–magnitude diagram of the GC candidates within $2R_e$.
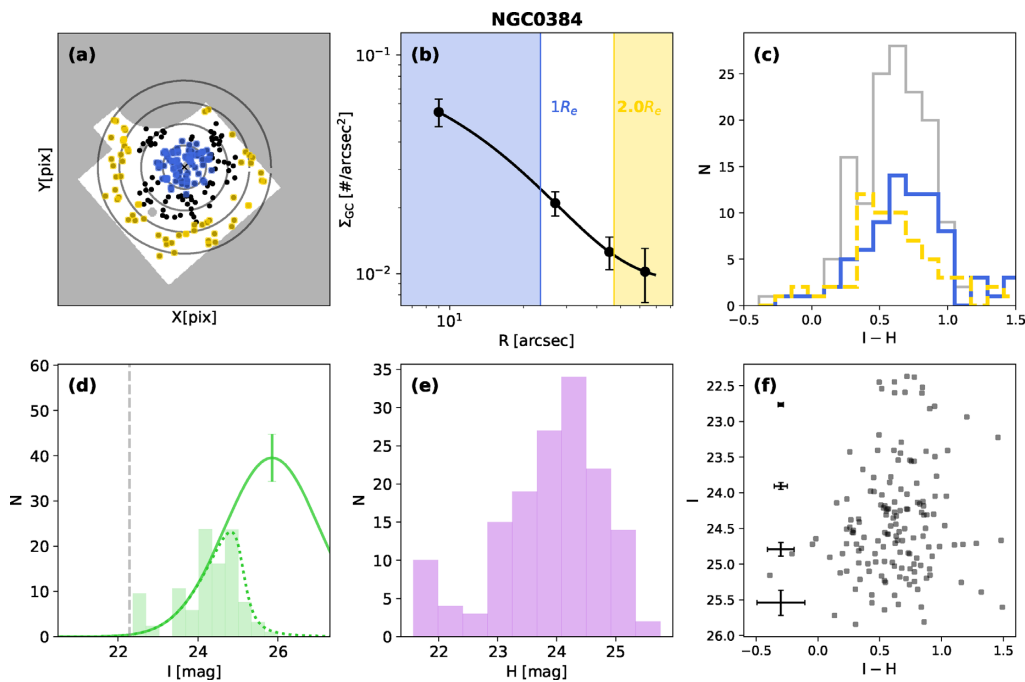
Figure A1. Derived parameters for the individual GCS of NGC 384; panel (a): the spatial distribution of the GC candidates highlighting with blue and yellow the sources belonging to the *inner* and *outer* population according to the Sérsic profile (panel b). The grey regions show masked areas due to bright stars, galaxies, and pixels with bad quality. The circles show the annuli on which the surface number density of GCs was determined. Panel (b): surface number density of the GC candidates as function of radius. The solid line shows the best Sérsic fit. Panel (c): $I - H$ colour distributions for the population within $1R_{e,GCS}$ (solid blue), outer to $2R_{e,GCS}$ (dashed yellow), and within $2R_{e,GCS}$ (solid grey). Panel (d): I-band luminosity function of the *inner* population corrected for contaminants. The dotted line shows the best Gaussian∗Pritchet function, the solid line is the corresponding single Gaussian. Panel (e): H-band luminosity function of the GC candidates within $2R_e$. Panel (f): $I - H$ versus I colour–magnitude diagram of the GC candidates within $2R_e$ with the mean error bars per magnitude bin.
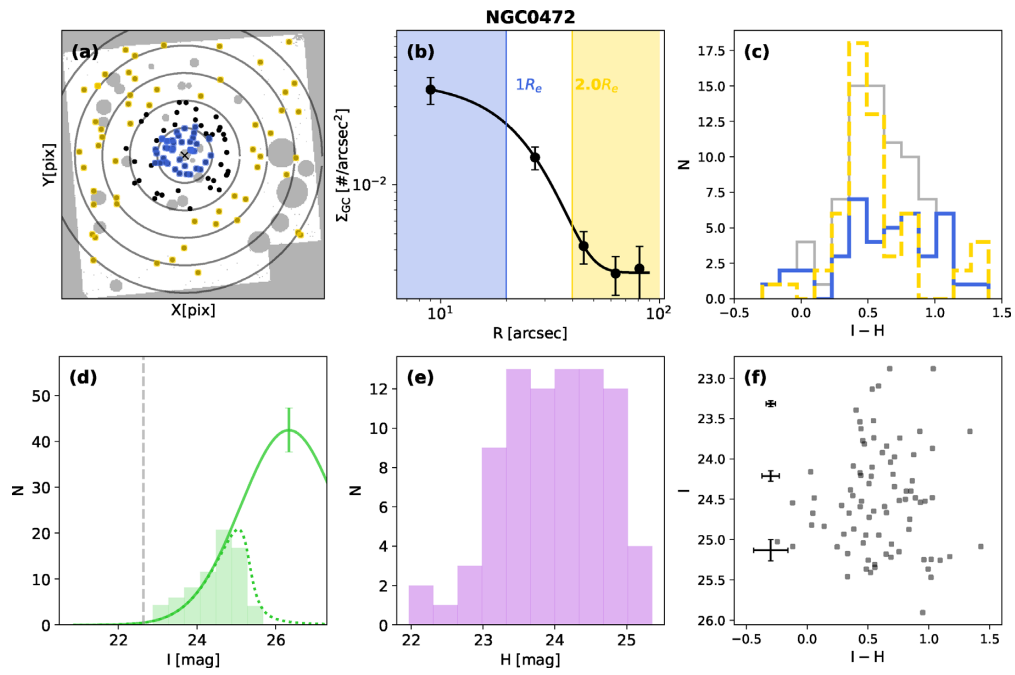
NGC0472

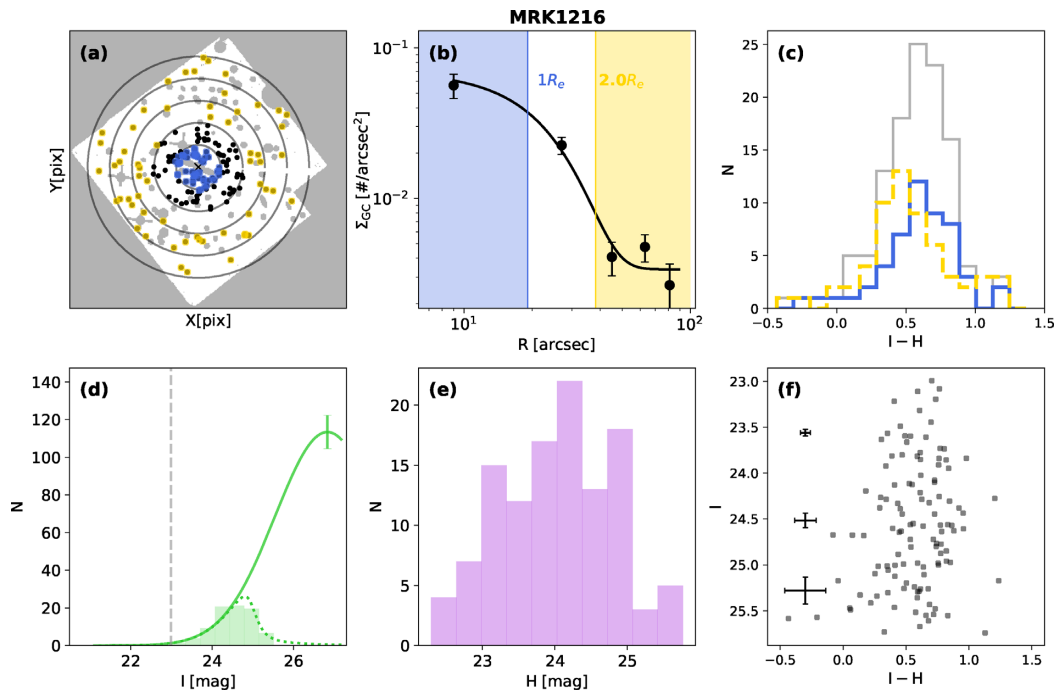**Figure A2.** Same as in Fig A1.

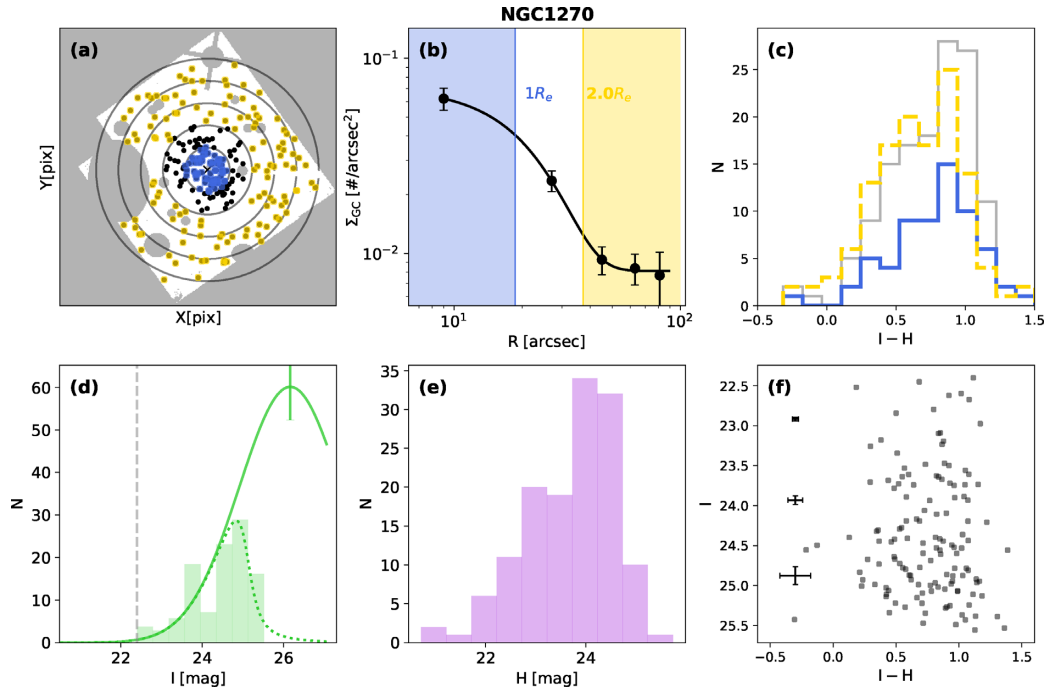**MRK1216**

Figure A3. Same as in Fig A1.
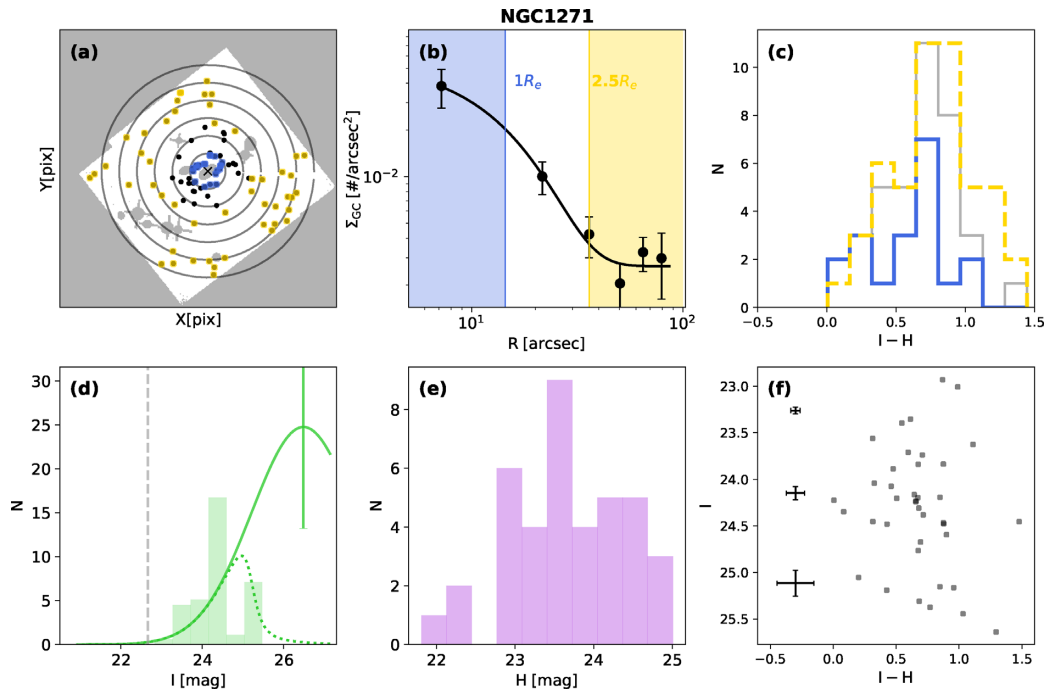
Figure A4. Same as in Fig A1.
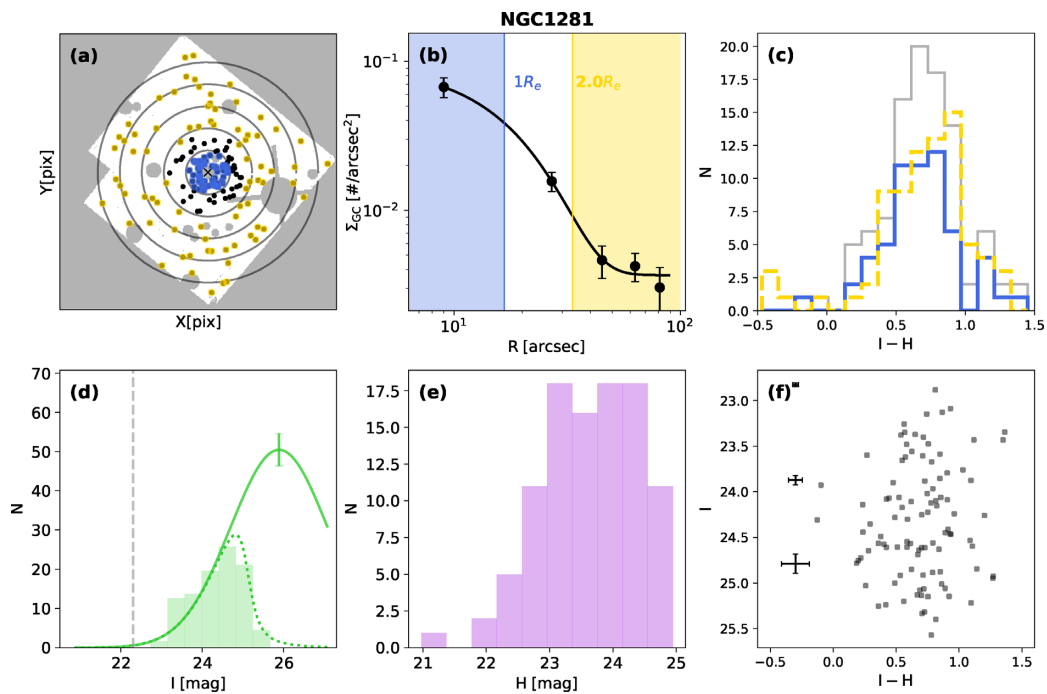

Figure A5. Same as in Fig A1.
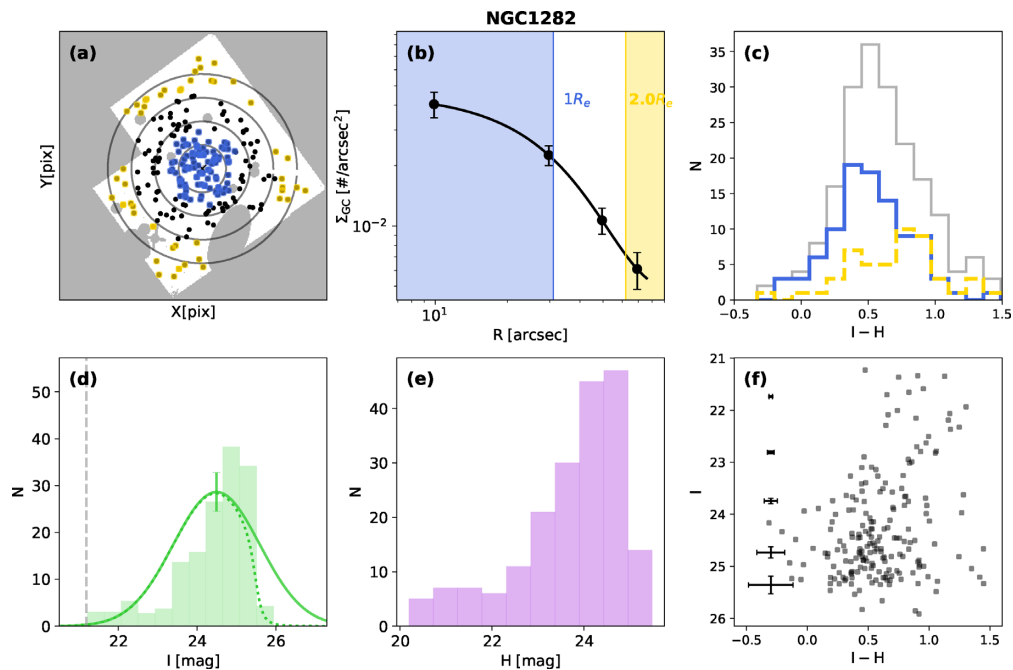
Figure A6. Same as in Fig A1.
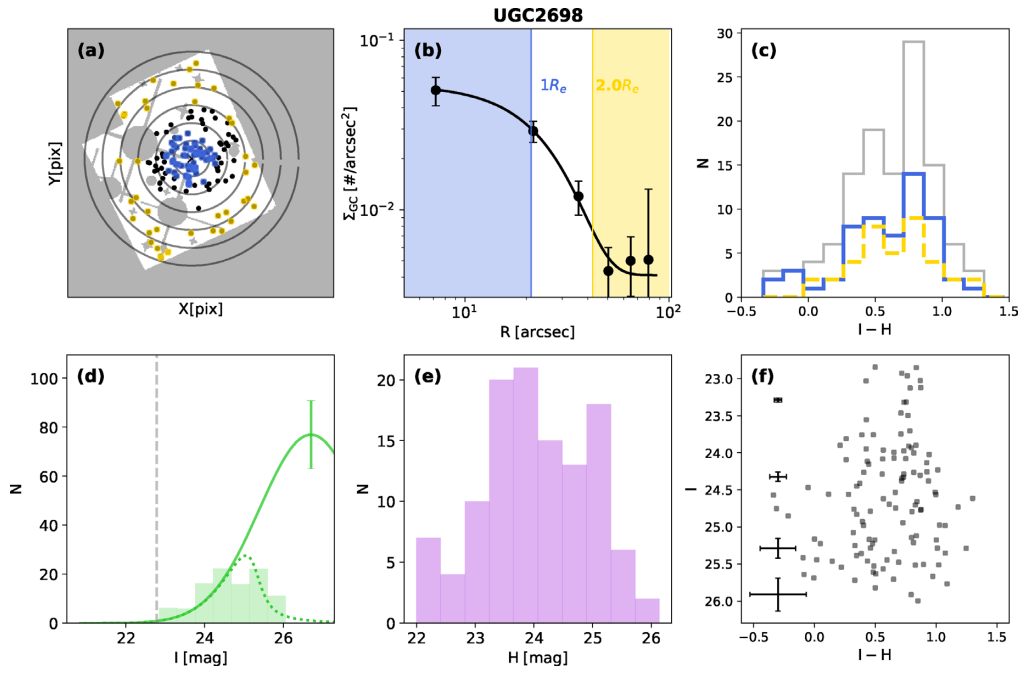

Figure A7. Same as in Fig A1.
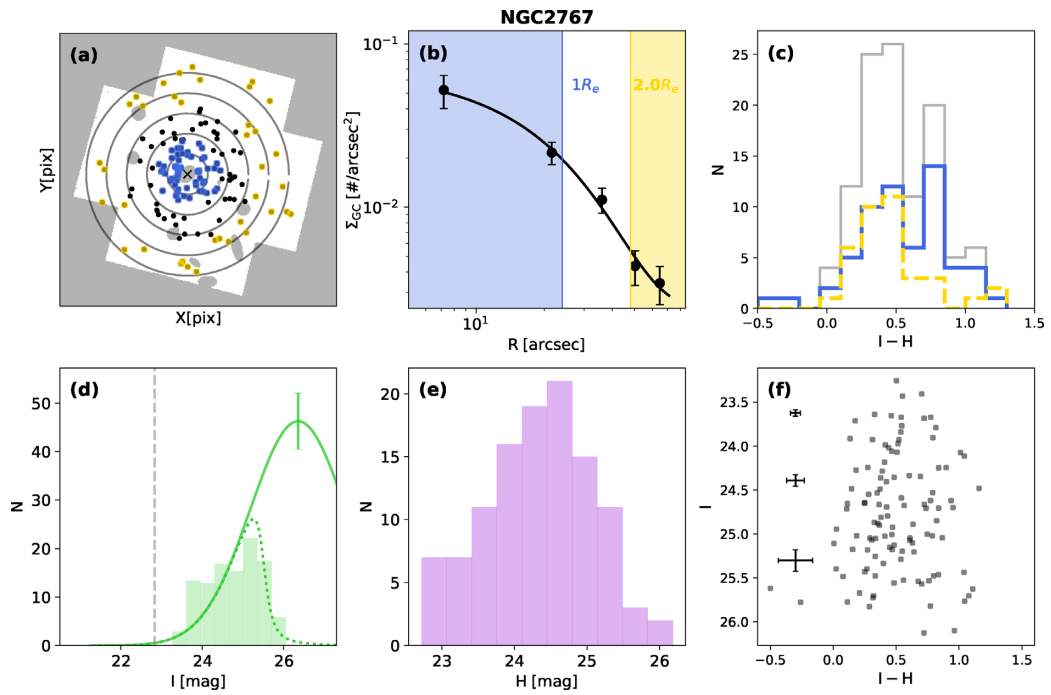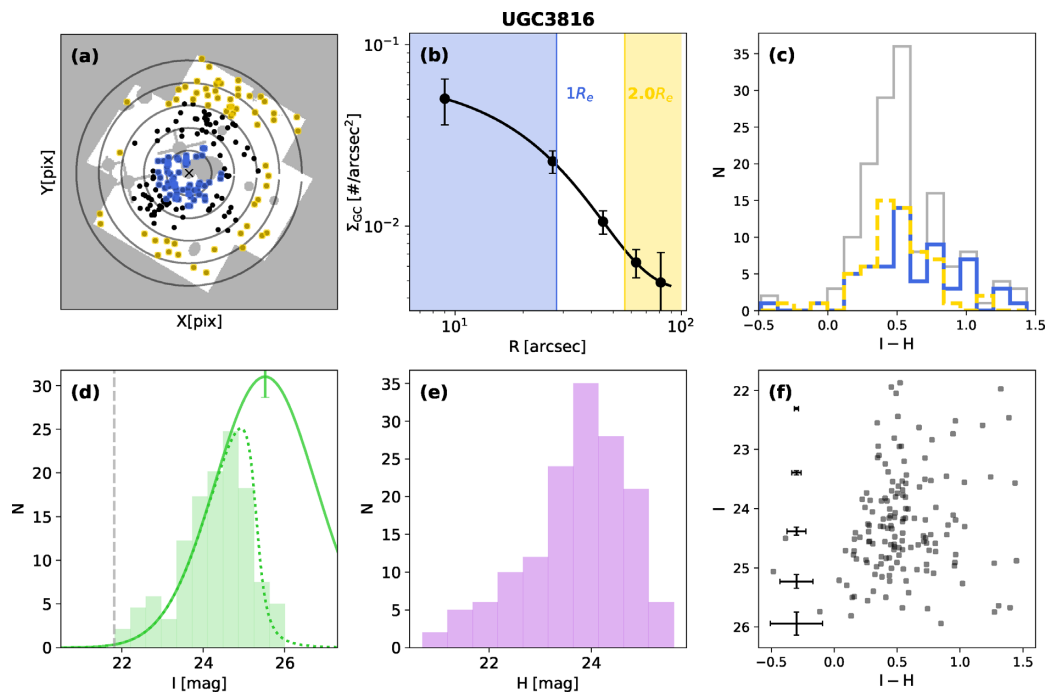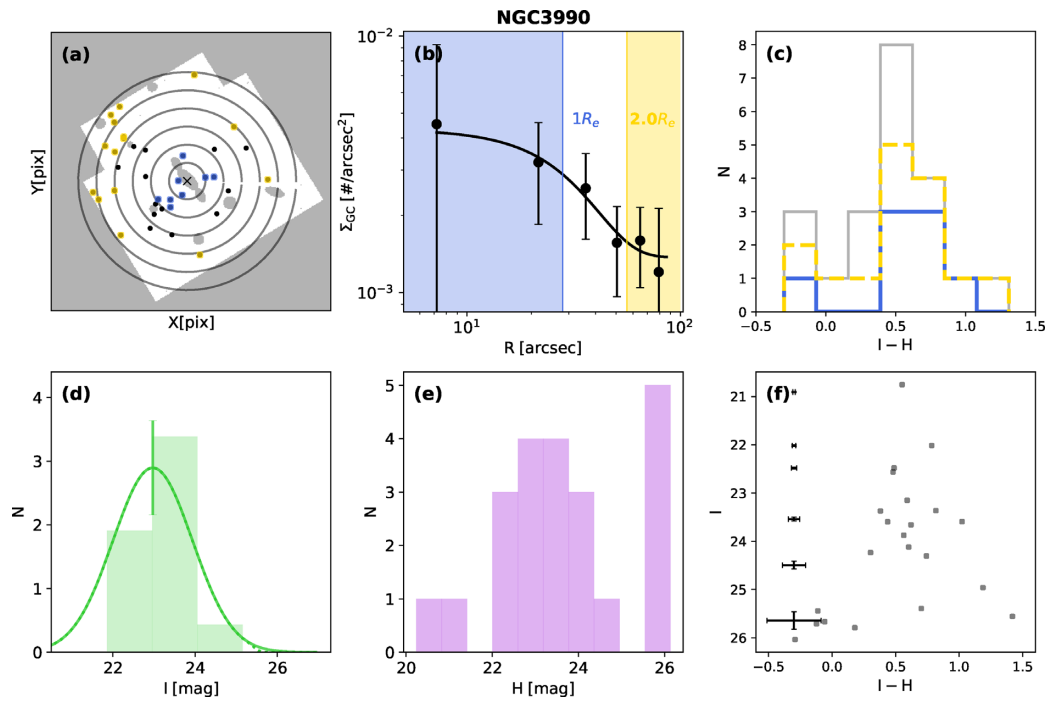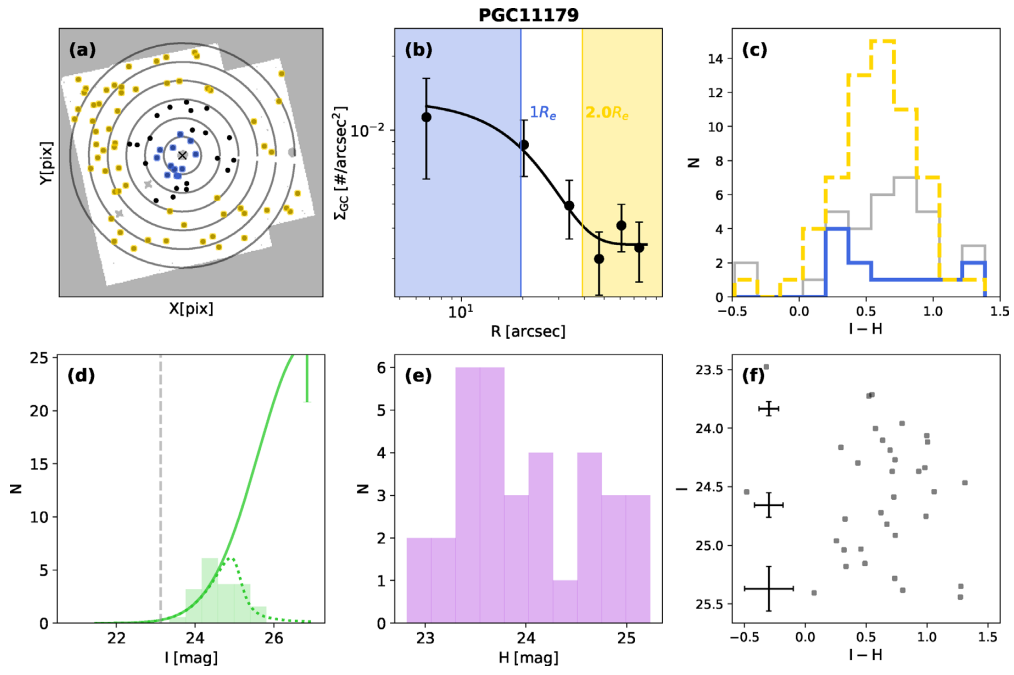
Figure A8. Same as in Fig A1.

Figure A9. Same as in Fig A1.

Figure A10. Same as in Fig A1.

Figure A11. Same as in Fig A1.

Figure A12. Same as in Fig A1.
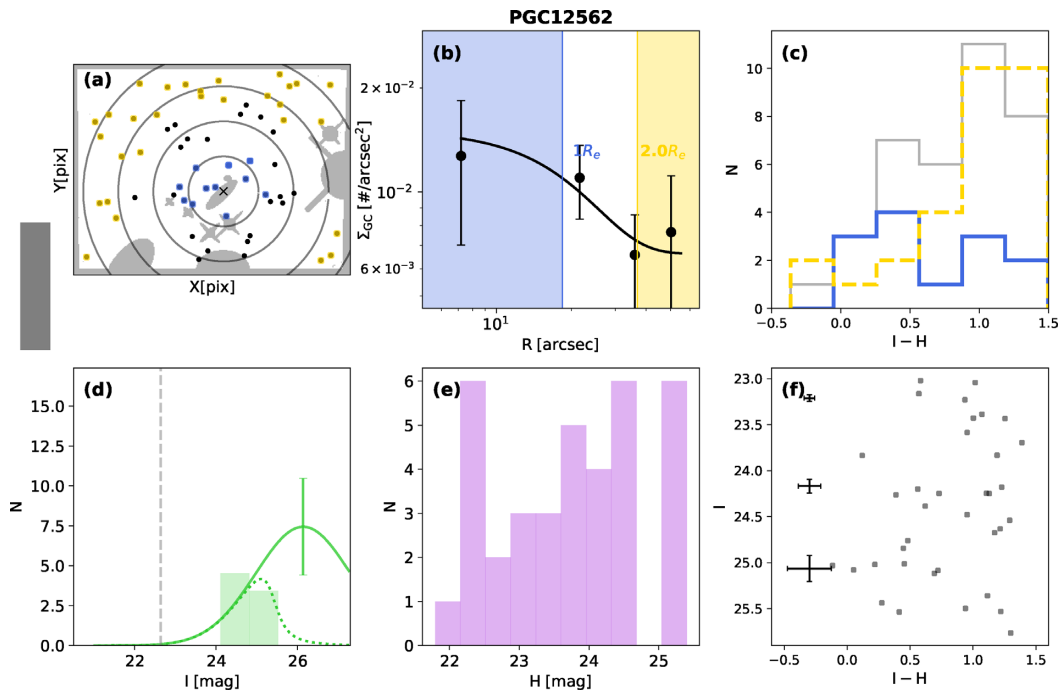
Figure A13. Same as in Fig A1.
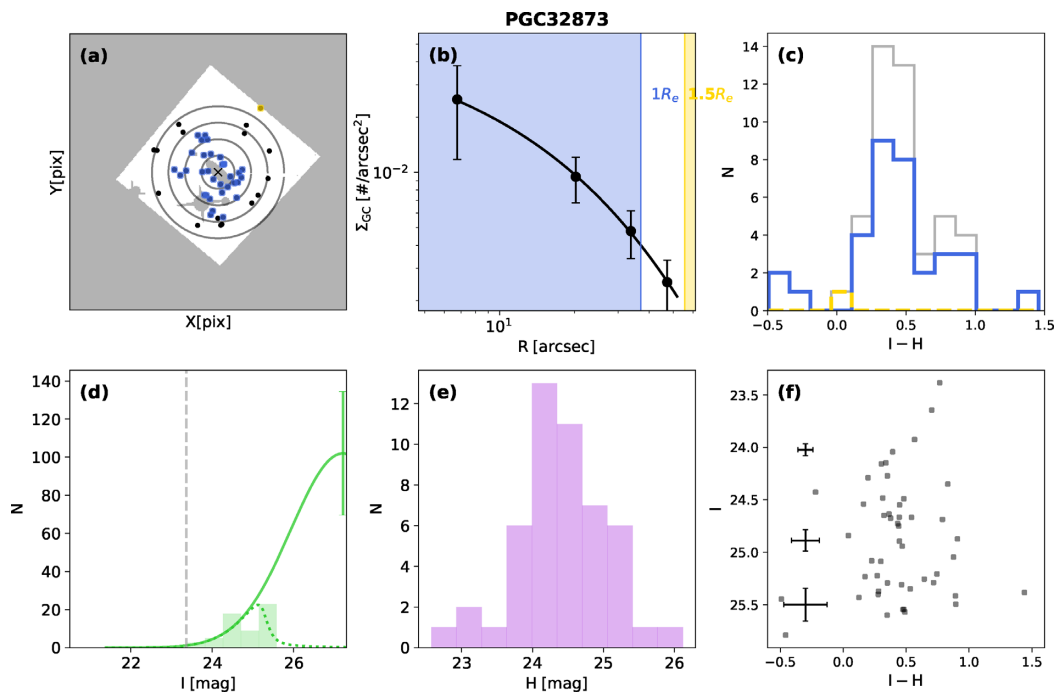
Figure A14. Same as in Fig A1.
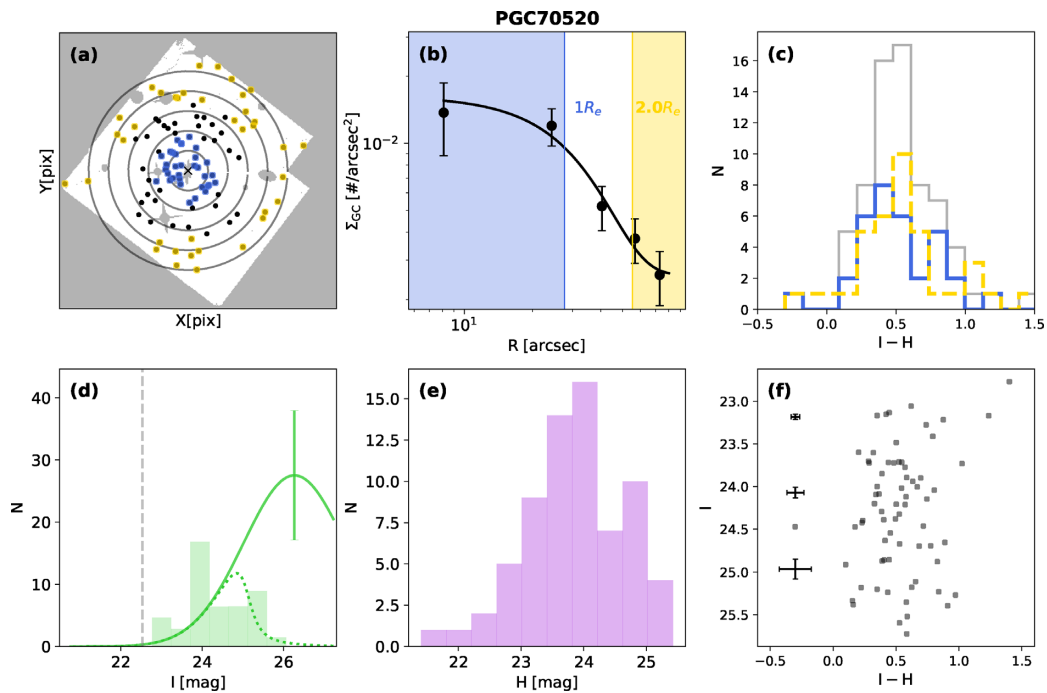
Figure A15. Same as in Fig A1.

This paper has been typeset from a TEX/LATEX file prepared by the author.